6-28-2018

Electronic Structure, Pore Size Distribution, and Sorption Characterization of an Unusual MOF, {[Ni(dpbz)][Ni(CN)$_4$]}n, dpbz = 1,4-bis(4-pyridyl)benzene

Winnie Wong-Ng
National Institute of Standards and Technology

Izaak Williamson
Boise State University

Matthew Lawson
Boise State University

Daniel W. Siderus
National Institute of Standards and Technology

Jeffrey T. Culp
Department of Energy

See next page for additional authors

Electronic structure, pore size distribution, and sorption characterization of an unusual MOF, $\{[Ni(dpbz)][Ni(CN)_4]\}_n$, dpbz = 1,4-bis(4-pyridyl)benzene

Winnie Wong-Ng,[1,a] Izaak Williamson,[2] Matthew Lawson,[2] Daniel W. Siderus,[1] Jeffrey T. Culp,[3,4] Yu-S. Chen,[5] and Lan Li[2]

[1]*Materials Measurement Science Division, National Institute of Standards and Technology, Gaithersburg, Maryland 20899, USA*
[2]*Department of Materials Science and Engineering, Boise State University, Boise, Idaho 83725, USA*
[3]*National Energy Technology Laboratory, Department of Energy, P.O. Box 10940, Pittsburgh, Pennsylvania 15236, USA*
[4]*AECOM, Pittsburgh, Pennsylvania 15236, USA*
[5]*ChemMatCARS, University of Chicago, Argonne, Illinois 60439, USA*

(Received 12 February 2018; accepted 24 May 2018; published online 26 June 2018)

The monoclinic $(Ni(L)[Ni(CN)_4]$ (L= 1,4-Bis(4-pyridyl) benzene) compound (defined as Ni-dpbz) is a flexible metal organic framework which assumes a pillared structure with layers defined by 2D $Ni[Ni(CN)_4]_n$ nets and dpbz ligands as pillars. The structure features an entrapped dpbz ligand that links between the open ends of four-fold Ni sites from two neighboring chains. This arrangement results in an unusual 5-fold pseudo square-pyramid environment for Ni and a significantly long Ni-N distance of 2.369(4) Å. Using Density Functional Theory calculations, the different bonding characteristics between the 5-fold and 6-fold Ni's were determined. We found that there is weak covalent bonding between the 5-fold Ni and N in the entrapped ligand, and the 6-fold Ni-N bonds provide effective electronic conduction. The disordered dimethyl sulfoxide (DMSO) solvent molecules are not bonded to the framework. The material has a single pore with a diameter of 4.1 Å. This pore includes approximately 55% of the total free volume (based on a zero-diameter probe). The accessible pore surface area and pore volume were calculated to be 507 m^2/g and 6.99 cm^3/kg, respectively. The maximum amount of CO_2 that can be accommodated in the pores after DMSO is removed was found to be 204 mg/g, agreeing with the results of adsorption/desorption experiments of about 220 mg/g. https://doi.org/10.1063/1.5025674

I. INTRODUCTION

Solid adsorption processes have been studied extensively in recent years as an effective and economical way for CO_2 capture and storage (CCS) technology.[1–4] Various types of porous solid sorbent materials, including porous coordination polymer (or metal organic frameworks, MOF), flexible MOF, and zeolites have been investigated worldwide.[5–24] Flexible MOFs are effective sorbents that possess both highly ordered network and structural transformability.[7,8,11,25–37]

The pillared layer motif is commonly used to design metal organic frameworks (MOFs). Materials based on the pillared cyano-bridged architecture, $[Ni'(L)Ni(CN)_4]_n$ (L = pillar organic ligands), have been shown to be remarkably versatile. By the precise control of the properties of the spacers, such as shape, functionality, flexibility, length, and symmetry, one can obtain materials containing diverse architectures and functions. In recent years, this synthetic strategy was expanded upon by Culp *et al.* who included a number of 1,4-bis-(4-pyridyl)benzene derivatives as pillaring linkers forming a family of ≈40 different porous coordination compounds collectively called pillared cyanonickelates or PICNICs.[7] Several PICNICs show flexible behaviour during the adsorption and desorption of guest molecules such as CO_2.[7,8] Flexible PICNICs and other soft porous crystals[26] change their structures in response to the adsorption and desorption of guests.[26–33] This transition between low porosity and high porosity structural phases (often referred to as a gating behavior) is dependent on pressure, temperature, and the nature of the guest.[11,34–37]

We have investigated the structure of a member of the PICNICS, the flexible $\{[Ni(1,4\text{-bis}(4\text{-pyridyl})benzene)][Ni(CN)_4]\}_n$ (defined as Ni-dpbz), which was synthesized using the modular MOF synthesis method.[19] The dpbz ligand is a linear chain consisting of a phenyl ring sandwiched between two pyridine rings. The structure of Ni-dpbz has been determined previously in our laboratory using the Advanced Photon Sources (APS) microcrystallography facility [Sector 15 (ChemMat CARS)].[38] The material is monoclinic $P2_1/c$, a= 6.7883(3) Å, b= 14.4840(7) Å, c= 28.9167(13) Å, β= 93.2950(10)°, V= 2838.4(2) Å^3, Z = 4, and D_x=1.42 g/cm^3.

The structure of Ni-dpbz, which is different from the conventional Hofmann compounds, is particularly interesting and unique. The salient structural feature of the Ni-dpbz material is the presence of additional dpbz ligands that link between two typically 4-fold $Ni(CN)_4$ sites. These "extra" pillar ligands occupy a fraction of the traditional Hofmann void space, and in this sense, behave like coordinated guest molecules. This arrangement is apparent in Fig. 1,[19] which shows the structure viewing down the crystallographic axis *b*, providing a clear view of how the two different dpbz ligands coordinate to the Ni ions in opposing 2D layers. One arrangement is the expected pillaring interaction of parallel

[a]Author to whom to correspondence should be addressed: Winnie.wong-ng@nist.gov. Tel. :301-975-5791.

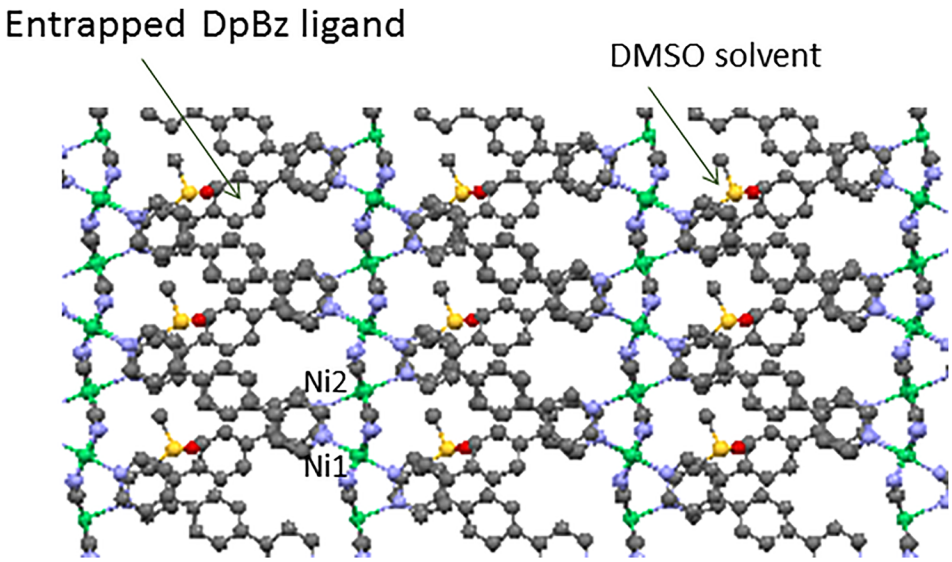

FIG. 1. A projection view of the structure down the crystallographic *b*-axis showing the parallel dpbz pillared ligands as well as the cross-linking of the ligand molecule connecting the Ni2 sites via longer Ni-N distance (green—Ni, blue—N, and grey—C). Reprinted with permission from W. Wong-Ng, J. T. Culp, Y.-S. Chen, J. R. Deschamps, and A. Marti, Solid State Sci. **52**, 1–9 (2016).

dpbz ligands connecting the Ni1 sites between the two $[Ni_2(CN)_4]_n$ layers, leading to the formation of the familiar 6-fold Ni1-N configuration. An unexpected dpbz chain connecting the two Ni2 sites via the N atoms of the pyridyl rings give rise to an unusual long N···Ni2 distance of 2.369(4) Å. In Fig. 2, an alternate view of the structure down the crystallographic axis "*a*" with the 2-D layers united by the dpbz ligands is illustrated. The entrapped solvent dimethyl sulfonyl oxide (DMSO) molecules are also shown. In this diagram, we also illustrate the 5- and 6-fold polyhedral coordination around Ni2 and Ni1, respectively. The extra dpbz chains occur as "trapped ligands." The resulting chemical formula for the compound is thus $Ni(dpbz)[Ni(CN)_4]\cdot{}^1/_2dpbz\cdot(0.44)DMSO$.

The present investigation highlights the bonding characteristics of Ni-dpbz. The three objectives of this study are (1) to use density functional theory (DFT) calculation to understand the bonding characteristics and charge distribution in dpbz, particularly around the N1 site (6-fold coordination) and N2 (5-fold coordination); (2) to conduct pore size characterization using modeling techniques, to estimate approximately the possible amount of CO_2 sorption, and to compare the results with experimental sorption experiments; and (3) to compare the pore feature of Ni-dpbz with another PICNIC compound, $Ni(L)[Ni(CN)_4]\cdot{}^1/_2L\cdot DMSO\cdot 2H_2O$, (where L = 1,2-bis(4-pyridyl)ethylene) (defined as Ni-bpene).[25] Ni-bpene also has an entrapped bpene ligand but is not bonded to the framework molecule.

II. COMPUTATIONAL AND EXPERIMENTAL APPROACHES

A. Computation methods

Two different computer modeling techniques were employed to obtain electronic structure, charge distribution, and pore characteristics in Ni-dpbz.

1. Structure and electronic calculations

As density function theory (DFT) methods have been shown to be successful for calculating structure and electronic properties of porous materials,[39] structure and electronic calculations were performed on Ni-dpbz using DFT and implemented with the Vienna *ab initio* simulation package (VASP) code.[40] Projector-augmented wave (PAW)[41] pseudopotentials were employed along with Perdew Burke Ernzerhof (PBE) exchange correlation functionals, implemented using the spin-polarized generalized gradient approximation (GGA).[42] A plane-wave basis set was used with a cutoff energy of 500 eV. Partial occupancies were handled with a Gaussian smearing of 0.005 eV. Brillouin zone integration for the electronic structure calculations was performed using a Γ-centered 8 × 4 × 2 *k*-point mesh. To address strong correlation effects from the Ni transition metal, an on-site Coulomb potential of $U_{Ni} = 8.0$ eV and an on-site exchange potential of $J_{Ni} = 1.0$ eV was applied following the DFT + U method.[43] Partial charge densities were calculated for the energy ranges of 1 eV below the Fermi level and 1.5 eV above the Fermi level to capture the valence band maximum (VBM) and conduction band minimum (CBM), respectively. These were subsequently mapped onto the relaxed structures and depicted as isosurface clouds. In order to better quantify the charge transfer between atoms, the Bader Charge Analysis program was also implemented.[44–47]

2. Computational pore size characterization

Computational methods were used to estimate the pore size distribution (PSD), skeletal porosity, gas-accessible pore volume, and the accessible surface area of Ni-dpbz. The chosen technique of computing the PSD was the method of Gelb and Gubbins[48] in which the local pore size at any given location in the material is equal to the diameter of the largest sphere containing that point without overlapping the material framework. The value of the PSD at a particular pore diameter is then the fraction of the free volume with local pore size equal to that diameter. We first reconstructed the Ni-dpbz material framework from the XRD crystal structure data, identified the coordinates of each atom in the framework, and followed by drawing of a van der Waals exclusion sphere around each atom (van der Waals radii were 1.63 Å for Ni, 1.20 Å for H, 1.70 Å for C, and 1.55 Å for N[49]). The PSD of the structure was then numerically calculated via the

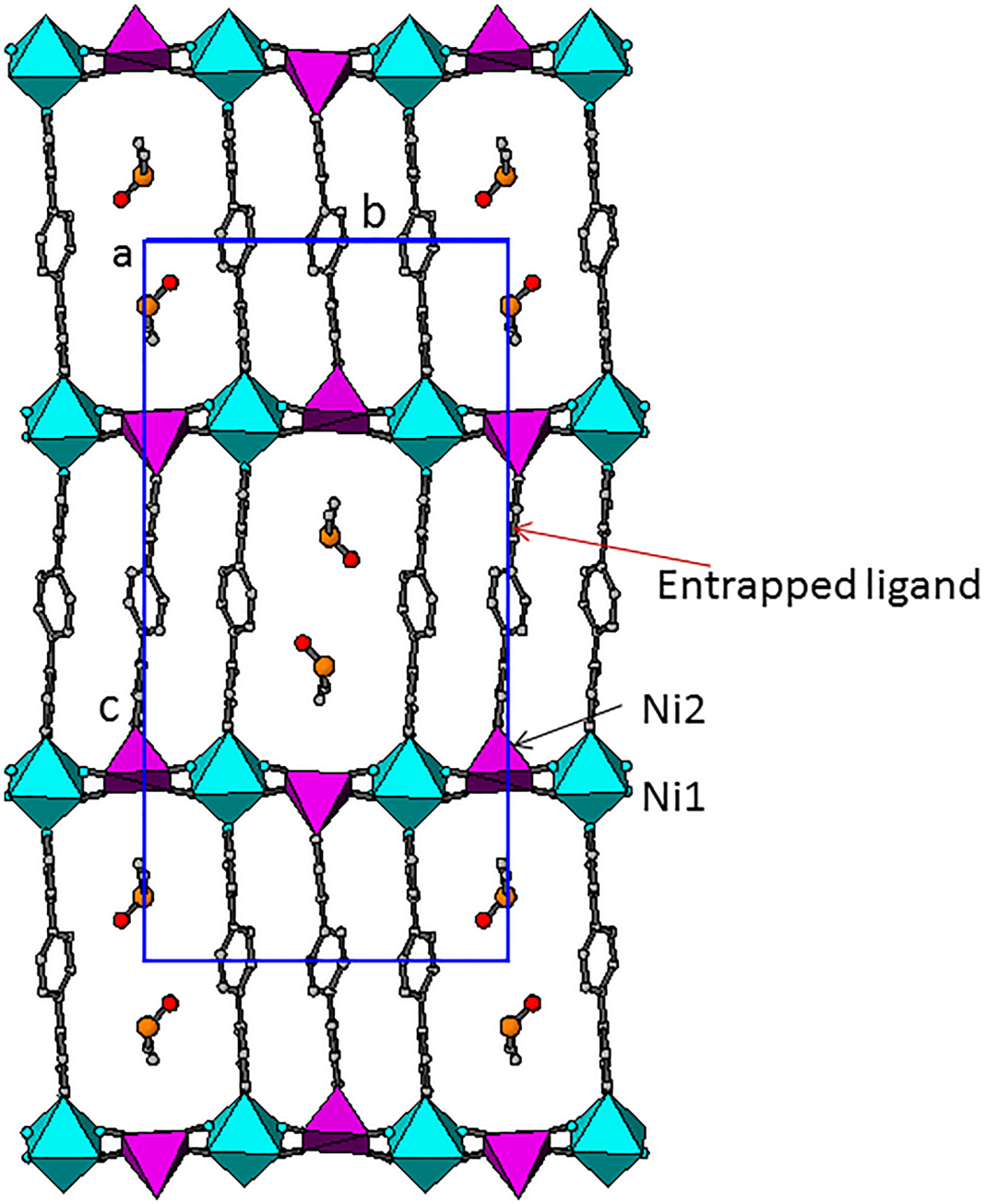

FIG. 2. Alternative polyhedral view of the octahedral and square-pyramidal coordination environments of Ni1 (blue) and Ni2 (pink), respectively, in Ni(dpbz)[Ni(CN)$_4$]. Reprinted with permission from W. Wong-Ng, J. T. Culp, Y.-S. Chen, J. R. Deschamps, and A. Marti, Solid State Sci. **52**, 1–9 (2016).

voxel technique described by Palmer *et al.*[50] using cubic voxels with side length of 0.1 Å or smaller. The PSD analysis was repeated using 10 unique realizations of the voxel grid and a final average PSD was computed from the ensemble of randomly generated grids. Uncertainty in the PSD was estimated using jackknife analysis.

The skeletal porosity (the volume fraction of the crystal unit cell not occupied by the van der Waals spheres surrounding each atom) and gas-accessible pore volume were also computed using the voxel technique. Essentially, the skeletal porosity is determined by counting the fraction of the unoccupied voxels identified in the PSD calculation. The gas-accessible pore volume is found by repeating the voxel analysis with a (molecular) nitrogen probe gas with assigned diameter of 3.681 Å. Voxels are deemed unoccupied if not covered by any sphere centered on a framework atom with radius equal to that atom's van der Waals radius plus the Nitrogen radius.

The surface area was characterized by the accessible surface area metric, as computed using the technique of Duren and coworkers[51] in which the framework atoms were assigned by the radii listed above and molecular N_2 was used as the probe gas. The use of N_2 with this diameter as the computational probe, is expected to yield an accessible surface area that correlates well with the BET surface area measured by N_2 adsorption.[52] As for the PSD, these analyses were repeated 10 times to allow jackknife error analysis.

To estimate the CO_2 capacity, a crude estimate which was not a N_2-based pore volume was used. The calculation is based on the free volume fraction from the pore-size

distribution calculation, which uses a zero-diameter probe. The maximum CO_2 capacity may be estimated, roughly, by representing CO_2 as a sphere with diameter of 4.2 Å (larger than C at 3.4 Å diameter and smaller than the major axis of 5.36 Å of CO_2), and then assuming the sphere can access all free volume with local pore size greater than 4.2 Å. This is, admittedly, a highly simplified estimate of the maximum sorption capacity; a more accurate and thermodynamically rigorous estimate could be obtained, for example, via molecular simulation. However, our objective here is a quick estimate based solely on the crystalline adsorbent structure and a minimal set of assumptions, in contrast to a more costly molecular simulation that would also require assignment of a tuned force field and atomic partial charges.

B. CO_2 adsorption and desorption isotherm measurements

Gravimetric CO_2 adsorption measurements were conducted on a Hiden IGA microbalance. The toluene extracted sample (~25 mg) was activated by heating under vacuum at 150 °C until the sample weight stabilized. Isotherms were then measured under flowing CO_2 regulated by a mass flow controller.[19] Equilibrium was determined at each pressure step using an internal fitting algorithm in the instrument control software. Buoyance corrections were then applied to the final equilibrium weights using known densities of all components in the sample and counter weight chambers from gas densities calculated using REFPROP.[53,54]

III. RESULTS AND DISCUSSION

A. Electronic structure and charge distribution

Using DFT, the calculated lattice constants for the unit cell are $a = 6.811$ Å, $b = 14.706$ Å, and $c = 29.115$ Å, while the cell angles were calculated as $\alpha = 90°$, $\beta = 93.569°$, and $\gamma = 90°$. These values were within 2% of experimental measurements [$a = 6.7883(3)$ Å, $b = 14.4840(7)$ Å, $c = 28.9167(13)$ Å, and $\beta = 93.2950(10)°$]. For the 6-fold coordinated Ni, the average Ni-N bond length was 2.094 Å while the Ni-N bond length for the 5-fold coordinated Ni was at 2.433 Å. This longer-than-average Ni-N bond length is consistent with the experimental measurements.

Electronic structure calculations further account for the difference in Ni-N bonding character for the 6- and 5-fold Ni (labeled Ni1 and Ni2, respectively). Figure 3 shows the total density of states (DoS, black) which project the local contributions from Ni (green) and N (blue) atoms in the structure. The dotted lines are for the 6-fold Ni1 sites and solid lines are for 5-fold Ni2 site. The overlap of Ni and N local density of states (LDoS) peaks for Ni1 and Ni2 indicate orbital hybridization and covalent character in the Ni-N bonds. The Ni and N atoms in the 6-fold coordination region have significant DoS in both bands in terms of peak intensities. However, the Ni and N in the 5-fold coordination region have relatively small DoS near the top of the valence band as compared to that of the 6-fold coordination region. Furthermore, the Ni1-N band is associated with more negative energy, implying bonding electrons are closer to the nucleus. On the other hand, the DoS peaks for the

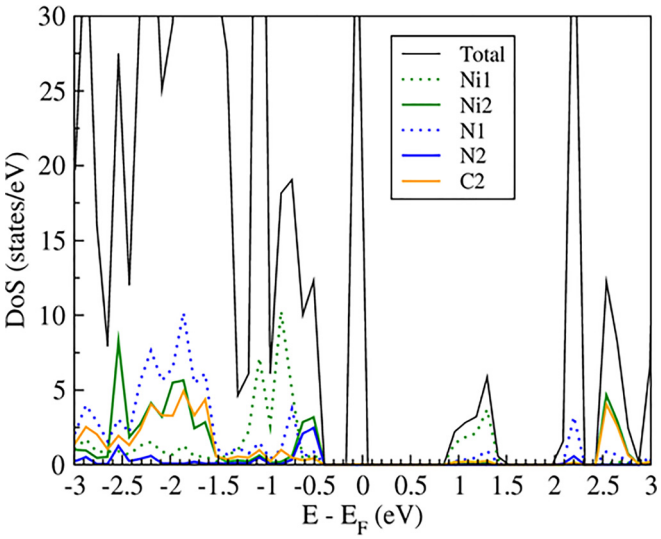

FIG. 3. Electronic local density of states (LDoS) plot for the Ni-dpbz system where the *x*-axis is shifted to $E_F = 0$ eV. The total density of states (DoS) is depicted with a thin black line, while the contributions from the Ni, N, and C atoms are depicted with green, blue, and orange lines, respectively. Dotted lines represent the data from atoms about the 6-fold coordinated Ni and associated N (labeled N1) and solid lines represent the contributions from atoms about the 5-fold coordinated Ni and associated N (labeled N2).

5-fold Ni2-N bonds are closer to the Fermi level (bonding electrons are in the outer shell). Therefore, Ni1-N bond is much stronger as compare to the Ni2-N bond, but the weak bond to the framework may enhance the stability of the structure. Since only Ni1-N (not Ni2-C) contributes to DoS states at the conduction band minimum (CBM), electron conduction occurs near Ni1 whereas the Ni2-N bonds do not have sufficient states in the conduction band to allow for electron conduction.

The bonding characteristics are also confirmed by the partial charge density maps for the valence band maximum (VBM) and conduction band minimum (CBM) states, as shown in Figs. 4 and 5, respectively. Conducting band minimum provides us information such as where electrons reside in excited states. These figures depict available charge states for a given energy range ($E - E_F = -1.0$ eV to 0 eV was used for the VBM and 0 eV to 1.5 eV was used for the CBM). The partial charge density at the VBM (shown as yellow isosurface clouds in Fig. 4) is localized around the Ni, S, and O atoms. Partial charge density at the CBM (yellow isosurfaces in Fig. 5) exists on the Ni1 atom and the C atom of the dpbz ligand, and on the two axial N atoms of the ligands which provide a bridge between Ni1 with the C atom of the dpbz ligand. Very little partial charge density is found in the four planar N connecting to Ni1 for the VMB and CBM, suggesting no conduction at the fermi energy. For the five-fold Ni2, the partial charge density accumulates only along the axial N of the ligand, and very little is found around Ni2. These diagrams suggest that Ni1 is much more effective than Ni2 in electron conduction.

Electronic charge transfer between atoms in a compound represents ionic bonding characteristics. Results from the Bader Charge Analysis program indicated that the average electronic charge transfer from Ni1 to N atoms is about 1.3 electrons per Ni1, while the average electron charge transfer from Ni2 to N atoms is about 0.94 electrons per Ni2. These

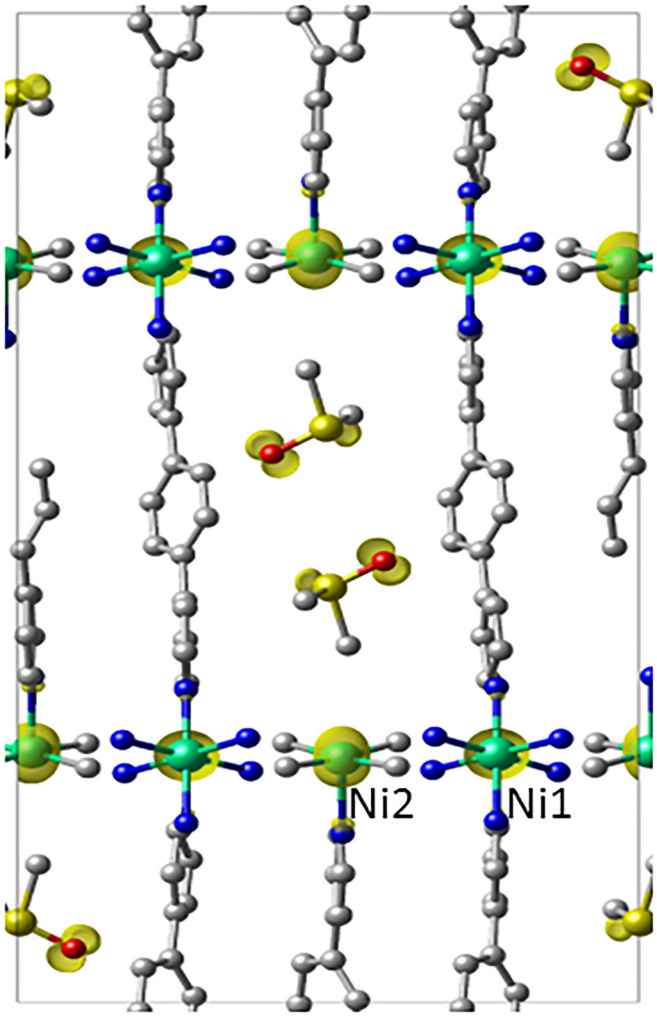

FIG. 4. A schematic of the structure is given with green—Ni, blue—N, grey—C, yellow—S, and red—O spheres. The partial charge densities are shown for the energy range of $-1.0\,\text{eV} \leq E - E_F \leq 0\,\text{eV}$ representing the VBM states. The corresponding partial charge densities are depicted as yellow isosurfaces.

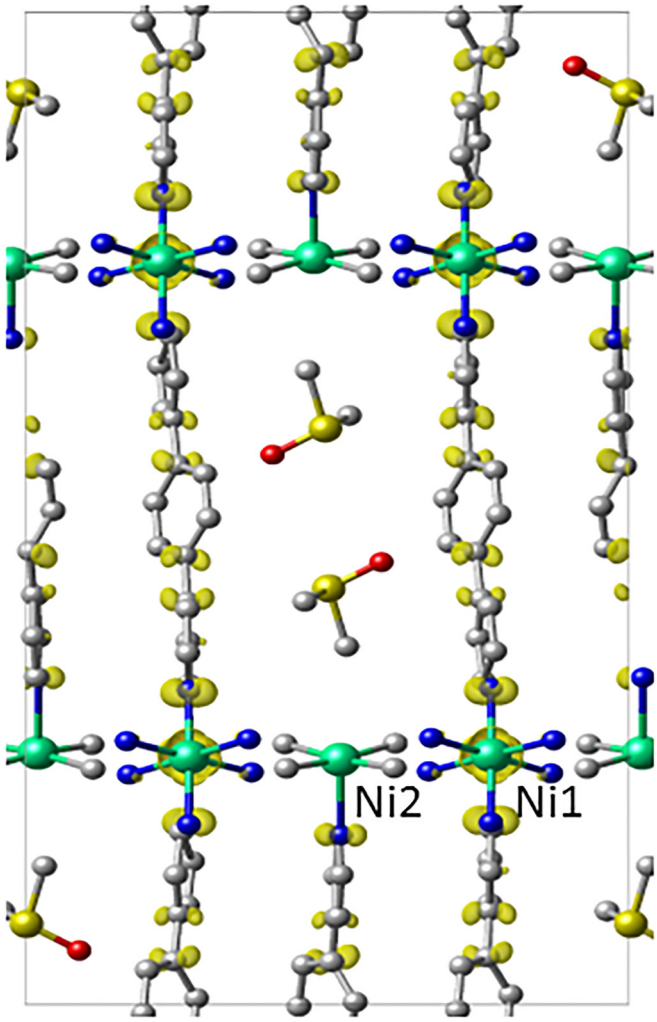

FIG. 5. A schematic of the structure is given with green—Ni, blue—N, grey—C, yellow—S, and red—O spheres. The partial charge densities are shown for the energy range of $0\,\text{eV} \leq E - E_F \leq 1.5\,\text{eV}$ representing the CBM states. The corresponding partial charge densities are depicted as yellow isosurfaces.

results suggest that the Ni1 bond has stronger ionic characteristics when compared to the Ni2 bond. We also found that electrons donated from Ni site to the neighboring N atoms are in turn transferred to the surrounding carbon atoms in the dpbz ligands.

B. Pore size distribution, skeletal porosity, gas-accessible surface area, and volume

Figure 6 displays a schematic representation of Ni-dpbz (based on the crystal structure data given in Table S1, with DMSO solvent removed), with van der Waals radii drawn about each constituent atom to indicate the approximate space taken up by the framework atoms. The schematic representation shows that Ni-dpbz has a single, rectangular pore channel. The skeletal porosity is approximately $40.68 \pm 0.002\%$ of the total volume. Our calculations based on a N_2 probe gas yield a gas-accessible pore volume of 0.00699 (12) cm^3/g and accessible surface area of 507.8 (2) m^2/g. Despite the not-insignificant skeletal porosity, the pore volume is rather small.

Pore size distribution of Ni-dpbz is given in Fig. 7. The material has a single pore with diameter approximately 4.1 Å. This pore includes approximately 55% of the total free volume (based on a zero-diameter probe). The remainder of the free volume is associated with pores with diameter

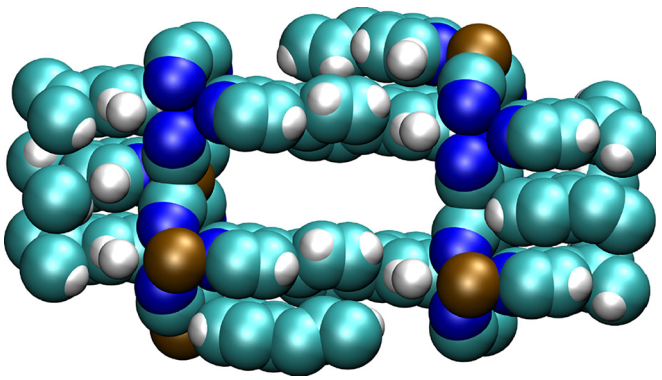

FIG. 6. Molecular structure of Ni-dpbz, with van der Waals exclusion volume of all atoms[44] shown by colored spheres. Atomic positions were obtained via the crystallographic information from this work, shown in Table S1. Color codes for atoms and molecules: cyan, C; white, H; brown, Ni; and blue, N.

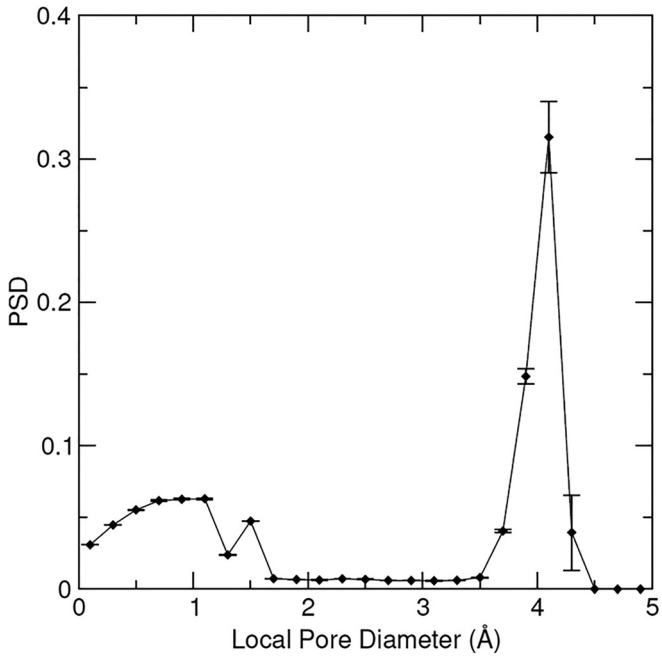

FIG. 7. Pore Size Distribution (PSD) of Ni-dpbz as a function of local pore diameter, as calculated by the method of Gelb and Gubbins[47] and described in the text. Error bars on the PSD are the estimates of the 95% confidence bounds computed via jackknife error analysis of 10 random realizations of the voxel grid.

below 1.70 Å, which is practically inaccessible to any guest species. The single pore has diameter not much larger than that of N_2 (3.861 Å) and, thus, provides little pore volume compared to more open structures. Also, given its rectangular shape, the pore has a large accessible surface area relative to its gas-accessible pore volume. This is comparable to narrow slit pores that have large area but accompanying low volume.

A comparison of the accessible volume and surface area of Ni-dpbz with a well-known rigid MOF (ZIF-8)[16] and another PICNIC compound Ni-Bpene[25] calculated using the same method is shown in Table I. Figure 8 gives the structure of Ni-Bpene with the presence of entrapped bpene ligands (DMSO molecules removed).[25] While both Ni-dpbz and Ni-bpene have similar Hoffman structure type and have entrapped ligands in the pores, the extra bpene ligands in Ni-bpene are not bonded to the framework. The pore volume and surface area of Ni-dpbz and of Ni-bpene are comparable, but they are much smaller than those in many reported open structures, with ZIF- 8 as an example.[16]

C. Adsorption/desorption isotherms

The Ni-dpbz compound after undergoing an activation procedure showed flexible behavior during the adsorption

TABLE I. Accessible pore volume and pore area for Ni-dpbz, Ni-bpene,[25] and ZIF-8.[16]

	Ni-dpbz	Ni-Bpene	ZIF-8
Accessible pore volume (cm^3/g)	0.00699	0.00990	0.172
Accessible pore area (m^2/g)	507.77	411.65	1459
# CO_2 molecules/unit cell	10.6	14.4	61.2

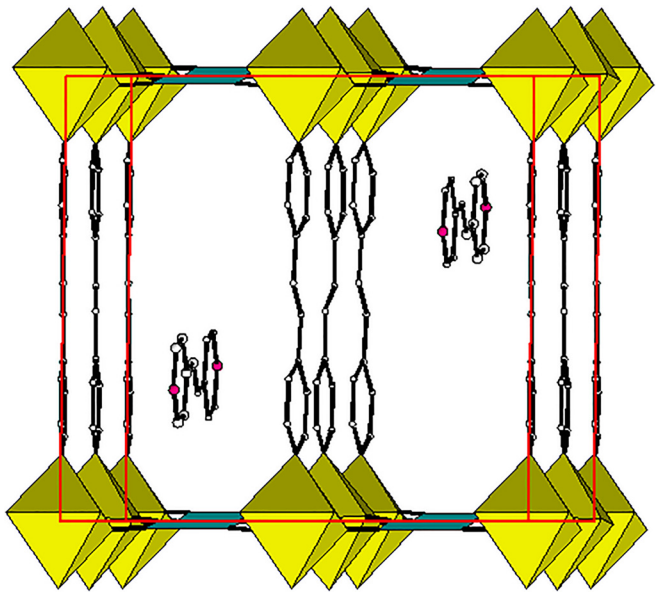

FIG. 8. Crystal structure of Ni-bpene showing the presence of an extra ligand in the unit cell. This ligand is not bonded to the framework molecule. The disordered DMSO solvent molecules are not shown.

and desorption of CO_2. The CO_2 isotherms of the Ni-dpbz crystals measured at 0 °C is shown in Fig. 9. A clear hysteresis loop indicates different adsorption curve and desorption curve. The y-axis pertains to the chemical formula including the extra dpbz ligand (but not the DMSO solvent molecules). The threshold pressure (P_{th}) (or gating pressure) associated with the pore opening transition illustrates the characteristics of a flexible MOF. The gating pressure associated with pore opening is about 8 bars. The saturation loading of CO_2 is about 220 mg/g at about 14 bars of CO_2. The maximum CO_2 capacity by representing CO_2 as a sphere of diameter of 4.2 A from the modeling technique has been calculated to be 204 mg/g (10.6 CO_2 per unit cell) for the DMSO-free structure, which compares reasonably well with the experimental data. A similar isotherm shape was also observed in Ni-bpene previously where the gating pressure is about 4–5 bars.[25]

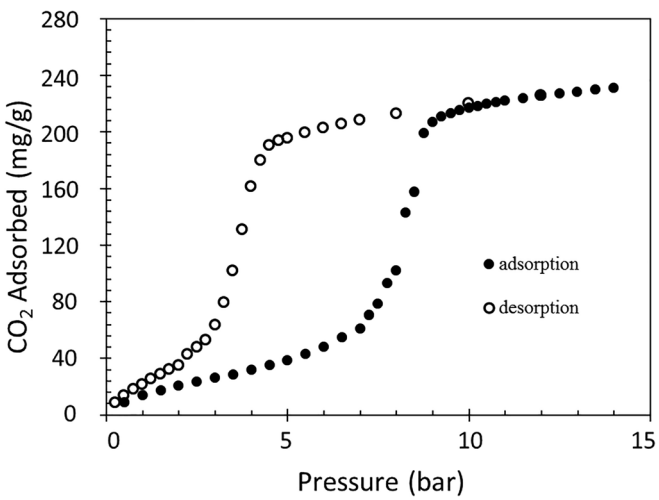

FIG. 9. CO_2 adsorption (solid symbols) and desorption (open symbols) isotherms at 10 °C for a crystalline sample of Ni-dpbz, where both the DMSO and the extra dpbz ligand have been removed (prepared as described in Ref. 7).

IV. CONCLUSION

Ni-dpbz is a flexible MOF that has an additional "entrapped ligand" in the structure. This extra dpbz ligand forms a weak bond to the four-fold coordinated Ni2 in the 2-D $Ni(CN)_4$ layer, resulting in an unusual five-fold square-pyramidal coordination (four Ni-C bonds and one exceptionally long Ni—N bond). From DFT calculations, the 6-fold Ni1 has stronger covalent bond and ionic bond characteristic, and provides a conduction bridge between the Ni and C atoms. The weak covalent bond of the extra dpbz ligand to the framework may enhance the stability of the structure.

The rectangular pores in the structure have a pore size of 4.1 A, accessible pore volume of 6.99 cm^3/kg, and large accessible surface area of 507 m^2/g. The fully CO_2 loaded phase corresponds to a loading of approximately 220 mg/g of $Ni(dpbz)[Ni(CN)_4]$ formula unit. We estimated the maximum CO_2 capacity to be 10.6 CO_2 per unit cell which is equivalent to 204 mg/g, agreeing well with the experimental data. Despite the small size of the cavities in the PICNIC type of compounds, their flexible structure features provide an opportunity to study their possible guest selectivity applications.

We plan to continue to understand the hysteresis loop in the sorption isotherms, the mechanism of the sorption process, and the structure/property relationship as a function of the partial pressure of CO_2 by using time-resolved *in situ* diffraction techniques.

SUPPLEMENTARY MATERIAL

See supplementary material for atomic coordinates and displacement parameters ($Å^2 \times 10^3$) for Ni-dpbz.

ACKNOWLEDGMENTS

ICDD is acknowledged for their partial financial support.

The purpose of identifying the equipment and software in this article is to specify the experimental procedure. Such identification does not imply recommendation or endorsement by the National Institute of Standards and Technology.

[1]D. M. Etheridge, L. P. Steele, R. L. Langenfelds, R. J. Francey, J. M. Barnola, and V. I. Morgan, J. Geophys. Res. Atmos. **101**, 4115, https://doi.org/10.1029/95JD03410 (1996).
[2]R. H. Gammon, E. T. Sundquist, and P. J. Fraser, in *Atmospheric Carbon Dioxide and the Global Carbon Cycle*, edited by J. R. Trabalka (U.S. Department of Energy, Washington, D.C., 1985), p. 25.
[3]J. Albo, P. Luis, and A. Irabien, Ind. Eng. Chem. Res. **49**, 11045 (2010).
[4]L. Espinal, D. L. Poster, W. Wong-Ng, A. J. Allen, and M. Green, Environ. Sci. Technol. **47**, 11960–11975 (2013).
[5]R. Chen, J. Yao, Q. Gu, S. Smeets, C. Baerlocher, H. Gu, D. Zhu, W. Morris, O. M. Yaghi, and H. Wang, Chem. Commun. **49**, 9500 (2013).
[6]S. S. Y. Chui, S. M. F. Lo, J. P. H. Charmant, A. G. Orpen, and I. D. Williams, Science **283**, 1148 (1999).
[7]J. T. Culp, C. Madden, K. Kauffman, F. Shi, and C. Matranga, Inorg. Chem. **52**, 4205–4216 (2013).
[8]J. T. Culp, M. R. Smith, E. Bittner, and B. Bockrath, J. Am. Chem. Soc. **130**, 12427 (2008).
[9]H. Furukawa, K. E. Cordova, M. O'Keeffe, and O. M. Yaghi, Science **341**, 1230444 (2013).
[10]W.-Y. Gao, M. Chrzanowski, and S. Ma, Chem. Soc. Rev. **43**, 5841 (2014).
[11]K. L. Kauffman, J. T. Culp, A. J. Allen, L. Espinal, W. Wong-Ng, T. D. Brown, A. Goodman, M. P. Bernardo, R. J. Pancoast, D. Chirdon, and C. Matranga, Angew. Chem. Int. Ed. **50**, 10888 (2011).
[12]V. Krungleviciute, K. Lask, L. Heroux, A. D. Migone, J. Y. Lee, J. Li, and A. Skoulidas, Langmuir **23**, 3106 (2007).
[13]J. Lee, J. Li, and J. Jagiello, J. Solid State Chem. **178**(8), 2527–2532 (2005).
[14]A. I. Skoulidas, J. Am. Chem. Soc. **126**, 1356 (2004).
[15]Q. M. Wang, D. M. Shen, M. Bulow, M. L. Lau, S. G. Deng, F. R. Fitch, and N. O. Lemcoff, Microporous Mesoporous Mater. **55**, 217 (2002).
[16]W. Wong-Ng, J. A. Kaduk, L. Espinal, M. R. Suchomel, A. J. Allen, and H. Wu, Powd. Diffr. **26**, 234 (2011).
[17]W. Wong-Ng, J. A. Kaduk, Q. Huang, L. Espinal, L. Li, and J. W. Burress, Microporous Mesoporous Mater. **172**, 95 (2013).
[18]W. Wong-Ng, J. A. Kaduk, H. Wu, and M. Suchomel, Powd. Diffr. **27**, 256 (2012).
[19]W. Wong-Ng, J. T. Culp, Y.-S. Chen, J. R. Deschamps, and A. Marti, Solid State Sci. **52**, 1–9 (2016).
[20]H.-H. Wang, L.-N. Jia, L. Hou, W-j Shi, Z. Zhu, and Y.-Y. Wang, Inorg. Chem. **54**, 1841 (2015).
[21]L.-Y. Du, W.-J. Shi, L. Hou, Y.-Y. Wang, Q.-Z. Shi, and Z. Zhu, Inorg. Chem. **52**, 14018–14027 (2013).
[22]D.-S. Li, J. Zhao, Y.-P. Wu, B. Liu, L. Bai, K. Zou, and M. Du, Inorg. Chem. **52**, 8091 (2013).
[23]D.-S. Li, Y.-P. Wu, J. Zhao, J. Zhang, and J. Y. Lu, Coord. Chem. Rev. **261**, 1 (2014).
[24]A. Schneemann, V. Bon, I. Schwedler, I. Senkovska, S. Kaskel, and R. A. Fischer, Chem. Soc. Rev. **43**, 6062–6096 (2014).
[25]W. Wong-Ng, J. T. Culp, J. Y. S. Chen, P. Zavalij, L. Espinal, D. W. Siderius, A. J. Allen, S. Scheins, and C. Matranga, CrystEngComm **15**, 4684 (2013).
[26]S. Horike, S. Shimomura, and S. Kitagawa, Nat. Chem. **1**, 695 (2009).
[27]S. Bureekaew, S. Shimomura, and S. Kitagawa, Sci. Technol. Adv. Mater. **9**, 014108 (2008).
[28]X. Chen, H. Zhou, Y.-Y. Chen, and A.-H. Yuan, Crystengcomm **13**, 5666 (2011).
[29]C. Gao, S. Liu, L. Xie, Y. Ren, J. Cao, and C. Sun, Crystengcomm **9**, 545–547 (2007).
[30]R. Kitaura, K. Fujimoto, S. Noro, M. Kondo, and S. Kitagawa, Angew. Chem. Int. Ed. **41**, 133 (2002).
[31]T. K. Maji, K. Uemura, H. C. Chang, R. Matsuda, and S. Kitagawa, Angew. Chem. Int. Ed. **43**, 3269 (2004).
[32]P. Song, B. Liu, Y. Li, J. Yang, Z. Wang, and X. Li, Crystengcomm **14**, 2296–2301 (2012).
[33]X.-F. Wang, Y. Wang, Y.-B. Zhang, W. Xue, J.-P. Zhang, and X.-M. Chen, Chem. Commun. **48**, 133–135 (2012).
[34]F.-X. Coudert, M. Jeffroy, A. H. Fuchs, A. Boutin, and C. Mellot-Draznieks, J. Am. Chem. Soc. **130**, 14294 (2008).
[35]V. Finsy, L. Ma, L. Alaerts, D. E. De Vos, G. V. Baron, and J. F. M. Denayer, Microporous Mesoporous Mater. **120**, 221 (2009).
[36]L. Hamon, P. L. Llewellyn, T. Devic, A. Ghoufi, G. Clet, V. Guillerm, G. D. Pirngruber, G. Maurin, C. Serre, G. Driver, W. van Beek, E. Jolimaitre, A. Vimont, M. Daturi, and G. Ferey, J. Am. Chem. Soc. **131**, 17490 (2009).
[37]E. Stavitski, E. A. Pidko, S. Couck, T. Remy, E. J. M. Hensen, B. M. Weckhuysen, J. Denayer, J. Gascon, and F. Kapteijn, Langmuir **27**, 3970 (2011).
[38]ChemMatCARS, Sector 15, Microdiffraction Facility, University of Chicago, Advanced Photon Source (APS), Argonne National Laboratory (ANL), Argonne, IL 60439, USA.
[39]P. Adhikari, M. Xiong, N. Li, X. Zhao, P. Rulis, and W. Y. Ching, J. Phys. Chem. C **120**, 15362–15368 (2016).
[40]G. Kresse and J. Furthmuller, "Efficient iterative schemes for ab initio total-energy calculations using a plane-wave basis set," Phys. Rev. B **54**, 11169 (1996).
[41]P. E. Blöchl, "Projector augmented-wave method," Phys. Rev. B **50**, 17953 (1994).
[42]J. P. Perdew, K. Burke, and M. Ernzerhof, "Generalized gradient approximation made simple," Phys. Rev. Lett. **77**, 3865 (1996).
[43]A. I. Liechtenstein, V. I. Anisimov, and J. Zaanen, "Density-functional theory and strong interactions: Orbital ordering in Mott-Hubbard insulators," Phys. Rev. B. **52**, R5467 (1995).
[44]W. Tang, E. Sanville, and G. Henkelman, "A grid-based Bader analysis algorithm without lattice bias," J. Phys.: Condens. Matter **21**, 084204 (2009).

[45]E. Sanville, S. D. Kenny, R. Smith, and G. Henkelman, "An improved grid-based algorithm for Bader charge allocation," J. Comput. Chem. **28**, 899–908 (2007).
[46]G. Henkelman, A. Arnaldsson, and H. Jónsson, "A fast and robust algorithm for Bader decomposition of charge density," Comput. Mater. Sci. **36**, 354–360 (2006).
[47]M. Yu and D. R. Trinkle, "Accurate and efficient algorithm for Bader charge integration," J. Chem. Phys. **134**, 064111 (2011).
[48]L. D. Gelb and K. E. Gubbins, Langmuir **15**(2), 305–308 (1999).
[49]A. Bondi, "van der Waals volumes and radii," J. Phys. Chem. **68**(3), 441–451 (1964); R. S. Rowland and R. Taylor, *ibid.* **100**(18), 7384–7391 (1996).
[50]J. C. Palmer, J. D. Moore, J. K. Brennan, and K. E. Gubbins, J. Phys. Chem. Lett. **2**(3), 165–169 (2011).
[51]H. Frost, T. Duren, and R. Q. Snurr, J. Phys. Chem. B **110**, 9565 (2006); T. Duren, F. Millange, G. Ferey, K. S. Walton, and R. Q. Snurr, J. Phys. Chem. C **111**, 15350 (2007).
[52]K. S. Walton and R. Q. Snurr, J. Am. Chem. Soc. **129**, 8552 (2007).
[53]E. W. Lemmon, M. L. Huber, and M. O. McLinden, NIST Standard Reference Database 23: Reference Fluid Thermodynamic and Transport Properties-REFPROP, Version 9.1, National Institute of Standards and Technology, Standard Reference Data Program, Gaithersburg, MD (2013).
[54]R. Span and W. Wagner, J. Phys. Chem. Ref. Data **25**, 1509 (1996).